This is the accepted manuscript made available via CHORUS. The article has been published as:

Identification of point defects using high-resolution electron energy loss spectroscopy

Shuo Wang, Katia March, Fernando A. Ponce, and Peter Rez

Phys. Rev. B **99**, 115312 — Published 18 March 2019

DOI: 10.1103/PhysRevB.99.115312

Identification of point defects using high-resolution electron energy loss spectroscopy

Shuo Wang[1], Katia March[2], Fernando A. Ponce[1], and Peter Rez[1]

[1.] Department of Physics, Arizona State University, Tempe, AZ 85287-1504, USA.
[2.] Eyring Materials Center, OKED, Arizona State University, Tempe, AZ 85287-1704, USA.

Abstract

Although there are many techniques that can detect bandgap states associated with point defects in the lattice, it is not routinely possible to determine the type of defect at submicron spatial resolution. Here we show that high-resolution electron energy loss spectroscopy (EELS) in a scanning transmission electron microscope can locate and identify point defects with a resolution of about 10nm in a wide-bandgap BAlN semiconductor. B interstitials, N vacancies, as well as other point defects have been experimentally detected using EELS and have been identified using density functional theory.

I. INTRODUCTION

It is well known that the electronic properties of semiconductors are determined by low concentrations of point defects, such as vacancies, interstitials, and impurities. There are many techniques that can be used to study changes in macroscopic properties such as conductivity and optical transitions brought about by point defects, but there are no reliable methods to characterize point defects at the nanometer scale. It has been reported that individual impurity atoms can be identified using Z contrast in scanning transmission electron microscopy (STEM) in 2D materials[1] or heavier atoms in a light atom matrix.[2] Techniques such as CL are limited to radiative defects and their spatial resolution is constrained by both beam broadening and carrier mobility. Even under the most favorable conditions for CL measurements made in a STEM the spatial resolution is no better than 20 nm.[3] Although high-resolution electron microscopy has revealed the atomic arrangements in line defects such as dislocations or planar defects such as grain boundaries or stacking faults,[4–8] it is unable to provide clear direct images of individual point defects due to the fact that images are projections through the entire specimen including its surfaces. The presence of point defects is usually inferred from indirect measures such as lattice distortions.[9] Although it is conceivable that they could be detected in tomographic reconstructions, it would be challenging to distinguish atoms close in atomic number,[10] and in general, it would not be possible to distinguish substitutional from interstitial impurity atoms.

In this report we show that we can distinguish point defects in BAlN thin films using monochromated electron energy loss spectroscopy (EELS) in a NION HERMES Ultra STEM microscope. Monochromation in the instrument allow us to achieve an energy resolution below 20 meV.[11] This is significant because it sufficiently lowers the background in the bandgap region, and makes it possible to detect states due to point defects. Taking advantage of this capability

Bowman *et al.* were able to detect bandgap states from Pr impurities in ceria.[12] Although the spatial resolution is degraded to about 10 nm due to delocalization arising from the long-range nature of the electromagnetic interaction, there is the possibility of locating defects with nanometer resolution by fitting the observed signal with the response function.

We focus our studies into the BAlGaN alloy system, where there currently is considerable interest in the incorporation of boron (B) into AlN and GaN for ultraviolet optoelectronic devices. The BAlGaN alloy system allows independent modification of the bandgap energy and the lattice parameter. BAlN with low B content can exhibit relatively large changes in the refractive index,[13] which can be of use in high reflectivity distributed Bragg reflectors based on BAlN/AlN thin film structures.[14] Theoretical studies also suggest higher light emitting efficiencies for BAlN active regions than for conventional AlGaN/AlN quantum wells.[15]

It is however difficult to obtain high quality BAlN alloys over a broad range of B compositions.[16–19] Recent reports show the possibility of synthesizing single-phase wurtzite BAlN thin films with a B concentration of up to 14%.[20,21] In this report we map the distribution of B and show, using high resolution EELS, that at high concentration B goes to interstitial sites, and that incorporation of B leads to other point defects such as N vacancies and Al vacancies and interstitials.

II. EXPERIMENTAL METHODS AND RESULTS

The BAlN films were grown by metalorganic chemical vapor deposition (MOCVD), with a B/(B+Al) gas-flow ratio of 0.12 and 0.18. The detailed growth process is described elsewhere.[20,21] The STEM specimens were prepared by mechanical wedge polishing and minimum ion milling. The ion-milling process was optimized to minimize the ion beam damage to the specimen surface. The ion-milling was performed using a Gatan Precision Ion Polishing

System. First the sample was thinned to electron transparency near the edge of the wedge, with Ar^+ ion beam energy of 4 keV, at a shallow angle of incidence. The beam energy was lowered to 2 keV to remove the surface damage layer. This approach is known to us to produce no discernable ion beam damage.[7] The region with least observable surface damage was chosen for STEM images and spectra. High-angle annular dark-field (HAADF) images were acquired at 100kV in the NION HERMES UltraSTEM 100 with a beam convergence semi-angle of 30 mrad. The minimum scattering angle accepted by the high angle detector was 80 mrad. Under these conditions it is well known that the image is only sensitive to atomic number.[22] Therefore, the image is not sensitive to inhomogeneities such as anti-phase/grain boundaries, which have been observed in the samples.[21] Each image was summed over 10 realigned individual images acquired with 32 μs/pixel. Figure 1(a) shows an atomic-resolution HAADF image near the BAlN/AlN interface, for the film with a B/(B+Al) gas-flow ratio of 0.12. The BAlN appears less homogenous than the AlN. The regions with higher B concentration appear darker, since the scattering cross section to the dark field detector is proportional to $Z^{1.7}$ for our geometry.[23] For comparison, Fig. 1(b) gives a HAADF image for BAlN/AlN grown with a higher B/(B+Al) gas-flow ratio of 0.18. The B concentration is estimated from the image intensity using the scattering cross sections listed in TABLE I.[24] There is considerable variation in the B concentration within each film. For the film with lower B concentration, it varies from 0.077 to 0.18, although the average of 0.12 is about the same as the gas ratio used during growth. Interestingly, the average of 0.16 for the film with higher B concentration is less than what would have been expected from the gas flow ratio of 0.18.

The high-resolution monochromated spectra from the high B concentration sample taken at 60kV are shown in Fig. 2(a). This acceleration voltage is needed to suppress the background in

the bandgap region caused by Cerenkov radiation. For AlN the threshold for Cerenkov radiation is 70kV,[25] and it would be higher for BAlN which has a lower refractive index. The spectra are collected for 20 secs with an energy dispersion of 7 meV per channel, with convergence and collection semi-angles of 28 and 35 mrad, respectively. The spectra show energy losses in the bandgap region. Although it is conceivable that these losses arise from optical phonons or guided light modes, this is not likely since the values would be at lower energies, as discussed in the Supplemental Material.[26] The features must be due to transitions from the valence band to defect levels just above the valence band, or from occupied defect levels just below the conduction band to empty conduction band states. As such, the onset marks a threshold with a tail toward higher energies. The thresholds are still detectable in the AlN substrate, although with diminishing intensity as the beam is moved further from the interface, as observed when comparing the series of scans marked in Fig. 2(b) and Supplemental Fig. 3.[26] This is not surprising, the long-range nature of the electromagnetic interaction for low energy dipole transitions from defect levels means that a signal is still detectable at a considerable distance (up to about 100 nm), as demonstrated for vibrational modes in guanine and phonon-polaritons in BN and SiO_2.[27–29] A model for the point spread function for the inelastic scattering process is needed to quantitatively assess the spatial resolution from a dipole transition. On the basis of a classical theory Egerton gives the following expression for the point spread function [30]

$$P(r) \propto \frac{exp\left(-\frac{2r}{b}\right)}{(r^2 + r_c^2)}, \tag{1}$$

where b is an "impact parameter" that can be related to the energy loss ΔE as

$$b = \frac{mv^2}{k\Delta E}, \tag{2}$$

where k is the electron wavevector, m is the electron mass and v is the electron velocity. The divergence at $r = 0$ is avoided using a cut off r_c, related to the probe convergence semi-angle θ_c,

$$r_c = \frac{1}{k\theta_c}. \quad (3)$$

On the other hand, a quantum mechanical treatment the point spread function gives[31]

$$P(r) \propto \frac{exp\left(-\frac{2r}{b}\right)}{\sqrt{(r^2 + r_c^2)}}. \quad (4)$$

One measure of the spatial resolution is the impact parameter, b, which is 150 nm for 0.3 eV transitions and 63 nm for 0.7 eV transitions. However the impact parameter over emphasizes the slow decay of the exponential tail in Eqns. 1 and 4. If we take the spatial resolution as the half width at half maximum of the function $P(r)$, i.e. r where $P(r) = \frac{1}{2}P(r = 0)$, we get 10 nm, which is in agreement with the experimental measurements shown in Fig. 2(a) and the profiles shown as Supplemental Fig. 3.[26]

The analytical theory for the spatial variation of the signal could be used in principle to fit the observed signal and localize the point defect with nanometer resolution, in a similar way to the techniques used in super-resolution optical microscopy.[32]

Note that there is no bandgap state observed in scan No 1 in Fig 2(a), acquired >200 nm away from the BAlN/AlN interface. This is evidence that the observed states are not correlated with surface damage induced by ion milling, because the ion beam cannot selectively damage BAlN but not AlN.

The threshold energies in the spectrum are numbered in Fig. 3(a) for a BAlN region in the specimen with high B concentration where they are most apparent. These features are less prominent in the spectrum from the specimen with lower B concentration in Fig. 3(b), where only thresholds marked 2, 3, and 5 are apparent. The threshold 1 becomes a shoulder on the tail

of zero-loss peak. No new thresholds appear in Fig. 3(b). A summary of the threshold positions is given as TABLE II.

III. THEORY AND DISCUSSION

To identify the origin of these features, calculations of densities of states with the VASP Density Functional Theory (DFT) code were used to explore whether postulated point defects give rise to states in the band gap, and whether transitions involving these states match experimental observations.[33,34] DFT has been previously applied to the calculation of the formation energy of various point defects in GaN and AlN, with the aim of understanding the origin of the observed luminescence.[35–39] If a state in the band gap is unoccupied, the EELS spectrum will show a threshold corresponding to the transitions from the top of the valence band, followed by a slow decrease due to excitation of electrons from lower energies in the valence band. A similar argument applies to occupied bandgap states. In this case the threshold corresponds to a transition to the lowest level in the conduction band. The slow decrease at higher energies arises from exciting electrons from the filled bandgap state to higher energy states in the conduction band.

VASP DFT calculations were performed using projection augmented wave, local-density approximation potentials for single Al, B and N interstitial atoms, single Al and N vacancies in a supercell constructed from 3x3x2 AlN unit cells, following Zhang and Li's calculation.[40] The structures were initially relaxed with 3x3x3 k points, and then a high-resolution DOS was calculated by smearing with a Gaussian, half width 50 meV, with 5x5x5 k points. The supercells are shown in Fig. 4.

The bandgap for AlN from the DOS shown in Fig. 5(a) is underestimated as 4.6 eV, as is typical for DFT. Calculations were performed for the case of a substitutional B atom, a B

interstitial, an Al interstitial, a N vacancy, and an Al vacancy. For convenience we have measured all energies from the top of the valence band. The calculation determines the Fermi level as the highest filled energy state. This has been marked by a vertical line on the plots shown as Fig. 5. However, it could be argued that this Fermi level is a consequence of the small supercell used in the calculation, and that the highest filled state for an isolated point defect is at the top of the valence band. This is supported by the calculation of an Al interstitial in a larger supercell comprising 5x5x3 AlN unit cells, where the Fermi level has shifted but the energy of transition is the same as the energy calculated with the smaller supercell (See Supplemental Fig. 4).[26] By convention, the Fermi level in a semiconductor is half way between the valence band maximum and the conduction band minimum at absolute zero, which implies that a charged defect will affect the electronic bands in its vicinity. The observed thresholds, all less than 1 eV would suggest that there are transitions from the valence band to levels close in energy. This is possible because the defect states are very delocalized, as shown by Laaksonen for the radial distribution functions for nitrogen vacancies.[38] Alternatively transitions from defect levels close to the conduction band to empty conduction band states are possible. The placement of the Fermi level by the DFT calculation suggests that these levels have a good chance of being filled when there is a high concentration of the defect. Given the close proximity of the relevant energy levels to either the valence band or conduction band, it could be argued that the DFT energies are reliable and the only problem is the band gap, which can be resolved with a "scissors" operator.[41] It is hard to justify the alternative procedure outlined in Laaksonen where the calculated energy difference from the valence band maximum is scaled by the ratio of the measured band gap to the calculated band gap.[38] Applying this procedure would also mean scaling energies in the conduction band, which would produce results inconsistent with inner

shell spectroscopy.[42] Ideally one would perform GW calculations to give a correct band gap,[43] but this is not practical for even the relatively small supercells considered here.

In our calculations, there are no bandgap states when B is substituted for Al, and the density of states is very similar to that of AlN, in agreement with the density functional calculations of Zhang and Li.[40] In all the other cases the VASP calculations showed states in the band gap, consistent with previous reports on point defects in AlN.[44] Possible transitions are summarized in TABLE III (and marked in Fig. 5). The thresholds 2 and 5, at 0.39 eV and 0.79 eV respectively, are attributed to B interstitials. The threshold at 0.39 eV is more likely to arise from isolated interstitial defects where the position of the Fermi level is dominated by the surrounding perfect AlN, while the threshold at 0.79 eV is consistent with the Fermi level calculated from the small supercell which might better represent dense clusters of interstitials. It is expected that both isolated and clustered B interstitials would be present in the high and low concentration B films, albeit with lower intensity in the lower concentration film, given that the solubility limit of B in AlN is reportedly 2.8%.[45] It would seem that the thresholds 3 and 4, at 0.53 eV and 0.6 eV, arise from N or Al vacancies, and possibly Al interstitials. Not surprisingly these thresholds attributed to displaced Al and N atoms are more likely in the film with higher B concentration. Although the formation energy for Al interstitials is higher than for Al vacancies,[39] the Al-rich growth condition and tensile strain generated by substitutional B atoms may facilitate the formation of Al interstitials. The DFT calculations were not able to identify a plausible transition for threshold 1, which is very prominent in Fig. 3. However it is unlikely to be a plasmon. If each B atom were responsible for one electron associated with a plasmon, the plasmon energy would be about 3 eV for the range of boron concentrations in our specimens.

We would like to emphasize that the main point of the paper is to show that monochromated EELS in the STEM can be used to detect and localize point defects. The defects can be identified with the help of DFT calculations. As such, BAlN represents a convenient materials system where we have applied these techniques. We wish to emphasize that until now the electron microscope has been for the most part "blind" to point defects.

IV. CONCLUSION

In summary, we have demonstrated that high-resolution electron loss spectroscopy can not only detect but also distinguish between different point defects. At present the spatial localization is limited to about 10 nm due to the long-range nature of the electromagnetic interaction. In principle, it should be possible to achieve sub-nanometer resolution since the spatial variation of the defect signal can be described by an analytic function. Defect states inside the band gap of BAlN films have been observed by low-loss EELS. DFT calculations identified the states as B and Al interstitials, and N and Al vacancies. The B interstitials may result from introducing a B content higher than the solubility of B in AlN. The increase in the densities of Al interstitials and N and Al vacancies may be a consequence of the defective microstructures caused by the increase in B content.

ACKNOWLEDGEMENT

The authors gratefully thank Dr. Xiaohang Li, Dr. Theeradetch Detchprohm, and Prof. Russell Dupuis for providing the samples used in this study. Shuo Wang was supported by the National Science Foundation (NSF) under DMR-1411022, and by the NSF and the Department of Energy under NSF CA No. EEC-1041895. We gratefully acknowledge the use of facilities within the Eyring Materials Center at Arizona State University.

References

[1] O.L. Krivanek, M.F. Chisholm, V. Nicolosi, T.J. Pennycook, G.J. Corbin, N. Dellby, M.F. Murfitt, C.S. Own, Z.S. Szilagyi, M.P. Oxley, S.T. Pantelides, and S.J. Pennycook, Nature **464**, 571 (2010).

[2] K. van Benthem, A.R. Lupini, M. Kim, H.S. Baik, S. Doh, J.-H. Lee, M.P. Oxley, S.D. Findlay, L.J. Allen, J.T. Luck, and S.J. Pennycook, Appl. Phys. Lett. **87**, 034104 (2005).

[3] A. Tararan, S. di Sabatino, M. Gatti, T. Taniguchi, K. Watanabe, L. Reining, L.H.G. Tizei, M. Kociak, and A. Zobelli, Phys. Rev. B **98**, 094106 (2018).

[4] D. Gerthsen, F.A. Ponce, and G.B. Anderson, Philos. Mag. A **59**, 1045 (1989).

[5] A. Vilà, A. Cornet, J.R. Morante, M. Loubradou, R. Bonnet, Y. González, L. González, and P. Ruterana, Philos. Mag. A **71**, 85 (1995).

[6] C.-C. Chen, C. Zhu, E.R. White, C.-Y. Chiu, M.C. Scott, B.C. Regan, L.D. Marks, Y. Huang, and J. Miao, Nature **496**, 74 (2013).

[7] R. Liu, A. Bell, F.A. Ponce, C.Q. Chen, J.W. Yang, and M.A. Khan, Appl. Phys. Lett. **86**, 021908 (2005).

[8] R. Sinclair, F.A. Ponce, T. Yamashita, D.J. Smith, R.A. Camps, L.A. Freeman, S.J. Erasmus, W.C. Nixon, K.C.A. Smith, and C.J.D. Catto, Nature **298**, 127 (1982).

[9] H. Kim, Y. Meng, J.-H. Kwon, J.-L. Rouviére, and J.M. Zuo, IUCrJ **5**, 67 (2018).

[10] Y. Yang, C.-C. Chen, M.C. Scott, C. Ophus, R. Xu, A. Pryor, L. Wu, F. Sun, W. Theis, J. Zhou, M. Eisenbach, P.R.C. Kent, R.F. Sabirianov, H. Zeng, P. Ercius, and J. Miao, Nature **542**, 75 (2017).

[11] O.L. Krivanek, T.C. Lovejoy, M.F. Murfitt, G. Skone, P.E. Batson, and N. Dellby, J. Phys. Conf. Ser. **522**, 012023 (2014).

[12] W.J. Bowman, K. March, C.A. Hernandez, and P.A. Crozier, Ultramicroscopy **167**, 5 (2016).

[13] S. Watanabe, T. Takano, K. Jinen, J. Yamamoto, and H. Kawanishi, Phys. Status Solidi C **0**, 2691 (2003).

[14] M. Abid, T. Moudakir, G. Orsal, S. Gautier, A. En Naciri, Z. Djebbour, J.-H. Ryou, G. Patriarche, L. Largeau, H.J. Kim, Z. Lochner, K. Pantzas, D. Alamarguy, F. Jomard, R.D. Dupuis, J.-P. Salvestrini, P.L. Voss, and A. Ougazzaden, Appl. Phys. Lett. **100**, 051101 (2012).

[15] S.-H. Park, W.-P. Hong, J.-J. Kim, B.-H. Kim, and D. Ahn, in *2017 Int. Conf. Numer. Simul. Optoelectron. Devices* (IEEE, 2017), pp. 77–78.

[16] V. Vezin, S. Yatagai, H. Shiraki, and S. Uda, Jpn. J. Appl. Phys. **36**, L1483 (1997).

[17] A.Y. Polyakov, M. Shin, M. Skowronski, D.W. Greve, R.G. Wilson, A. V. Govorkov, and R.M. Desrosiers, J. Electron. Mater. **26**, 237 (1997).

[18] C.H. Wei, Z.Y. Xie, J.H. Edgar, K.C. Zeng, J.Y. Lin, H.X. Jiang, C. Ignatiev, J. Chaudhuri, and D.N. Braski, MRS Proc. **537**, G3.79 (1998).

[19] G. Orsal, N. Maloufi, S. Gautier, M. Alnot, A.A. Sirenko, M. Bouchaour, and A. Ougazzaden, J. Cryst. Growth **310**, 5058 (2008).

[20] X. Li, S. Wang, H. Liu, F.A. Ponce, T. Detchprohm, and R.D. Dupuis, Phys. Status Solidi B **254**, 1600699 (2017).

[21] S. Wang, X. Li, A.M. Fischer, T. Detchprohm, R.D. Dupuis, and F.A. Ponce, J. Cryst. Growth **475**, 334 (2017).

[22] D.B. Williams and C.B. Carter, *Transmission Electron Microscopy: A Textbook for Materials Science*, 2nd ed. (Springer, New York, 2009), pp. 379-381.

[23] M.M.J. Treacy, Microsc. Microanal. **17**, 847 (2011).

[24] P. Rez, Microsc. Microanal. **7**, 356 (2001).

[25] L. Gu, V. Srot, W. Sigle, C. Koch, P. van Aken, F. Scholz, S.B. Thapa, C. Kirchner, M. Jetter, and M. Rühle, Phys. Rev. B **75**, 195214 (2007).

[26] See Supplemental Material at [] for information about HAADF images, discussion on optic phonons and guided light modes, a figure demonstrating spatial resolution, and a calculation for a larger supercell, including Refs 46-51.

[27] P. Rez, T. Aoki, K. March, D. Gur, O.L. Krivanek, N. Dellby, T.C. Lovejoy, S.G. Wolf, and H. Cohen, Nat. Commun. **7**, 10945 (2016).

[28] O.L. Krivanek, T.C. Lovejoy, N. Dellby, T. Aoki, R.W. Carpenter, P. Rez, E. Soignard, J. Zhu, P.E. Batson, M.J. Lagos, R.F. Egerton, and P.A. Crozier, Nature **514**, 209 (2014).

[29] K. Venkatraman, P. Rez, K. March, and P.A. Crozier, Microscopy **67**, i14 (2018).

[30] R.F. Egerton, Ultramicroscopy **180**, 115 (2017).

[31] C. Dwyer, Private Communication.

[32] B. Huang, M. Bates, and X. Zhuang, Annu. Rev. Biochem. **78**, 993 (2009).

[33] G. Kresse and J. Furthmüller, Phys. Rev. B **54**, 11169 (1996).

[34] G. Kresse and D. Joubert, Phys. Rev. B **59**, 1758 (1999).

[35] T. Mattila and R.M. Nieminen, Phys. Rev. B **54**, 16676 (1996).

[36] T. Mattila and R.M. Nieminen, Phys. Rev. B **55**, 9571 (1997).

[37] D. Alden, J.S. Harris, Z. Bryan, J.N. Baker, P. Reddy, S. Mita, G. Callsen, A. Hoffmann, D.L. Irving, R. Collazo, and Z. Sitar, Phys. Rev. Appl. **9**, 1 (2018).

[38] K. Laaksonen, M.G. Ganchenkova, and R.M. Nieminen, J. Phys. Condens. Matter **21**, 015803 (2009).

[39] C. Stampfl and C.G. Van de Walle, Phys. Rev. B **65**, 155212 (2002).

[40] M. Zhang and X. Li, Phys. Status Solidi B **254**, 1600749 (2017).

[41] G.A. Baraff and M. Schlüter, Phys. Rev. B **30**, 3460 (1984).

[42] P. Rez and D.A. Muller, Annu. Rev. Mater. Res. **38**, 535 (2008).

[43] F. Aryasetiawan and O. Gunnarsson, Reports Prog. Phys. **61**, 237 (1998).

[44] H. Ye, G. Chen, Y. Zhu, and J. Zhang, Acta Phys. Sin. **56**, 5376 (2007).

[45] C.H. Wei and J.H. Edgar, J. Cryst. Growth **208**, 179 (2000).

[46] N. Bonnet, N. Brun, and C. Colliex, Ultramicroscopy **77**, 97 (1999).

[47] J.C. Nipko and C.-K. Loong, Phys. Rev. B **57**, 10550 (1998).

[48] M. Schwoerer-Bohning, A.T. Macrander, M. Pabst, and P. Pavone, Phys. Status Solidi B **215**, 177 (1999).

[49] P.A. Crozier, Ultramicroscopy **180**, 104 (2017).

[50] A. Yurtsever, M. Couillard, and D.A. Muller, Phys. Rev. Lett. **100**, 217402 (2008).

[51] L. Gu, V. Srot, W. Sigle, C. Koch, P. van Aken, F. Scholz, S.B. Thapa, C. Kirchner, M. Jetter, and M. Rühle, Phys. Rev. B **75**, 195214 (2007).

TABLE I. Boron concentration, x, at specific places indicated in Fig. 1. The x values are estimated from the Z contrast in HAADF images, assuming an intensity dependence $I(x)/I_{AlN} = \sigma(x)/\sigma_{Al} = 1 - x \cdot (1 - \sigma_B/\sigma_{Al})$. The scattering cross section σ for Al, B, and N are 15.27, 2.373, and 4.433 x10^{-4} Å^2, respectively.[24]

B/(B+Al) = 0.12			B/(B+Al) = 0.18		
	$I(x)$	x		$I(x)$	x
AlN average	2.23	0	AlN average	11.5	0
BAlN average	2.01	12%	BAlN average	9.90	16%
1	2.08	7.7%	4	9.49	20%
2	2.06	9.1%	5	10.4	11%
3	1.88	18%	6	10.2	13%

TABLE II. Summary of low-energy features in the BAlN EELS spectra in Fig. 3. The peaks are assigned to defects according to the relative positions of valence band maximum (VBM), conduction band minimum (CBM), and defect states summarized in TABLE III.

Peak #	Energy (eV)	Possible defect
1	0.27	Not assigned
2	0.39	B interstitial
3	0.53	N vacancy or Al vacancy
4	0.60	Al interstitial
5	0.79	B interstitial

TABLE III. Summary of proposed transitions from DFT calculations. Each state shows its energy (in eV) above the VBM. Only the states allowing transitions are taken into consideration when assigning the peaks.

Point defect	Defect transitions		
B interstitial	VBM → A	B → C	C → CBM
	0.4	0.18	0.8
Al interstitial	D → E	E → F	
	1.2	0.6	
N vacancy	VBM → G	H → I	I → CBM
	0.35	0.35	0.52
Al vacancy	VBM → J		
	0.55		

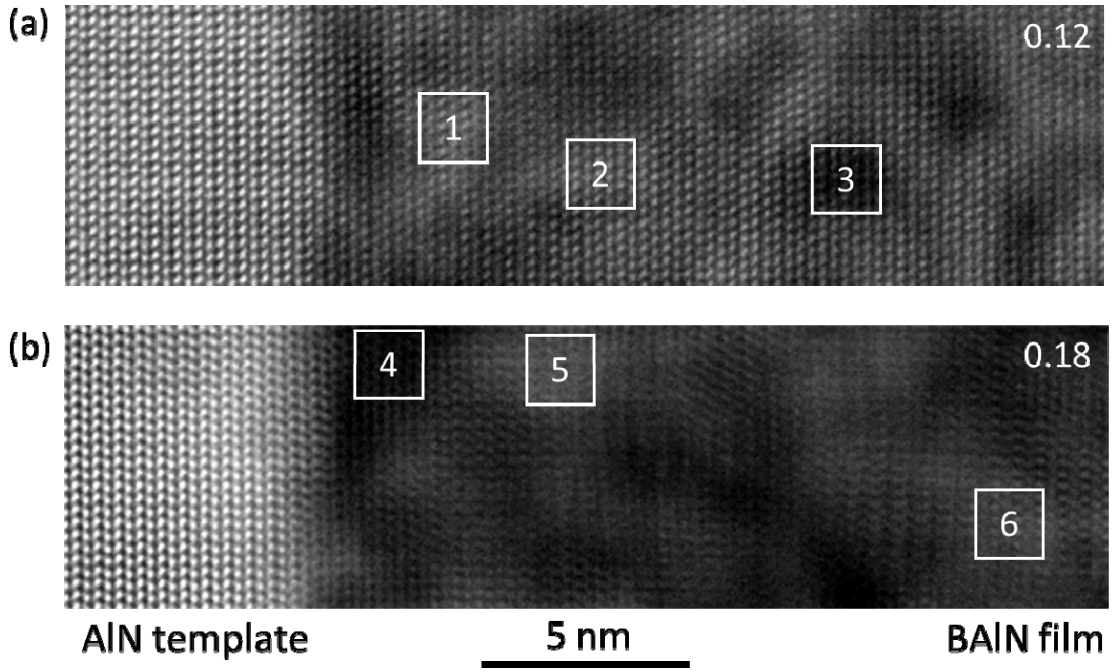

FIG. 1. HAADF images of AlN/BAlN heterostructures, with a B/(B+Al) ratio of: (a) 0.12, and (b) 0.18. The B concentrations in the numbered regions are estimated from the Z contrast and are listed in TABLE I.

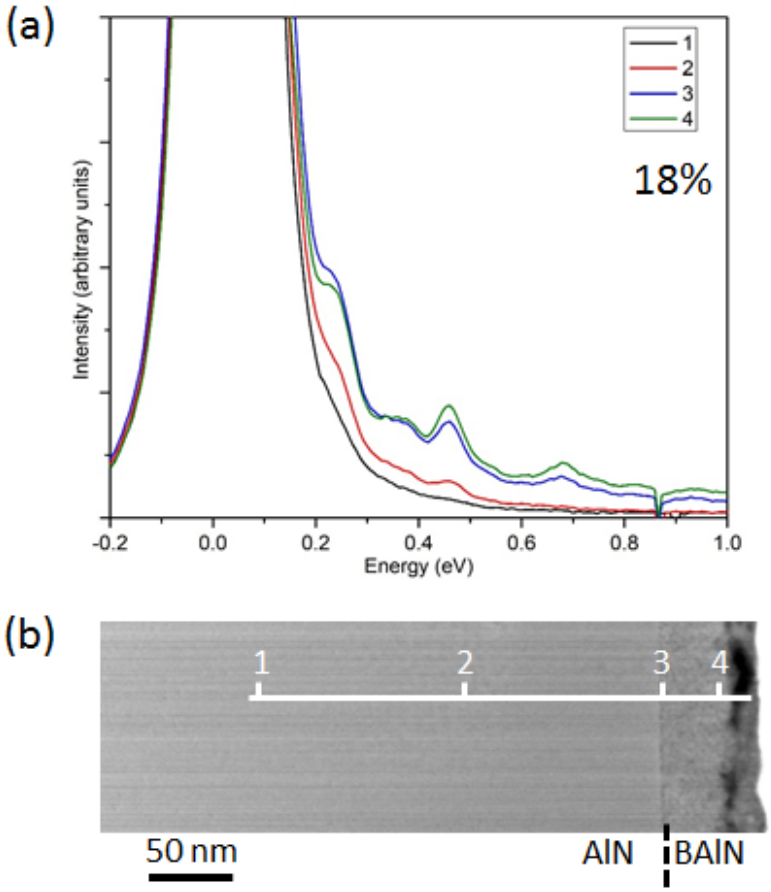

FIG. 2. (a) EELS low-loss spectra in the energy range below 1 eV of the sample with B/(B+Al) = 0.18. (b) HAADF image showing the positions where the spectra in (a) were acquired. The Z contrast of this image is poor for BAlN/AlN interface, under this certain acquisition condition.

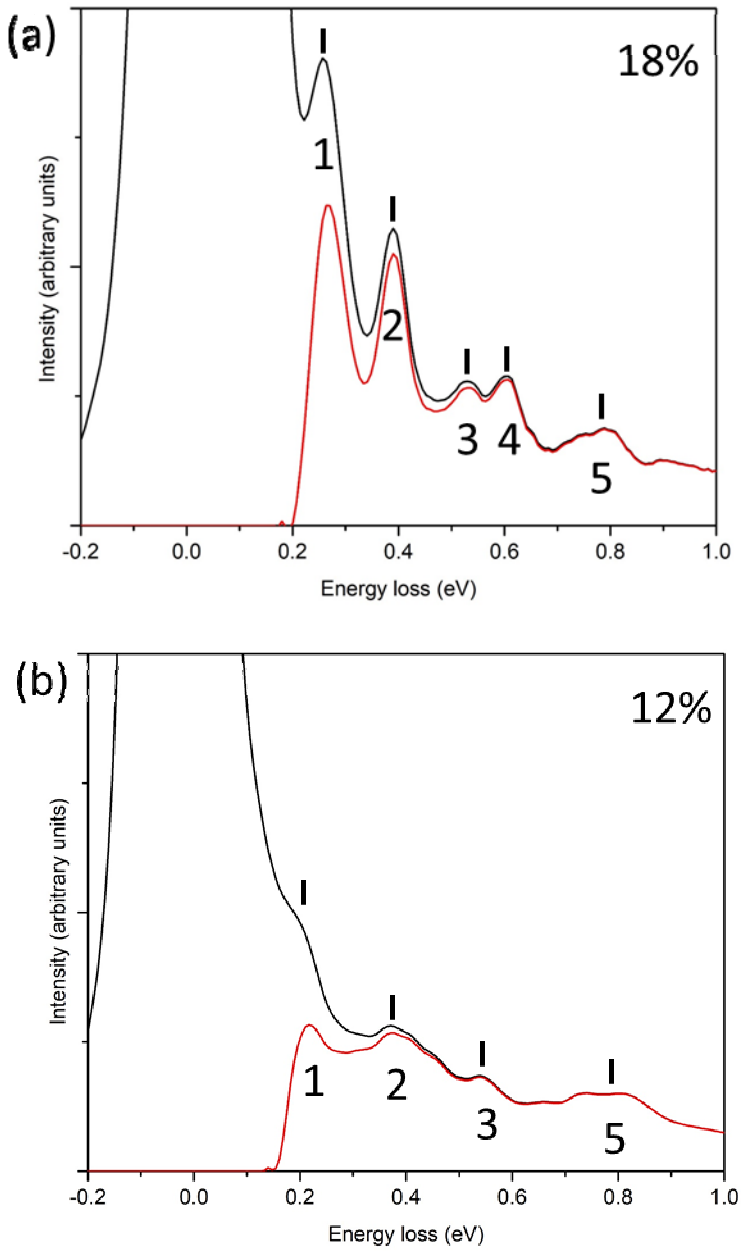

FIG. 3. EELS low-loss spectra of a scanned region in the BAlN films with B/(B+Al) (a) 0.18 and (b) 0.12, with background-subtracted spectra shown in red.

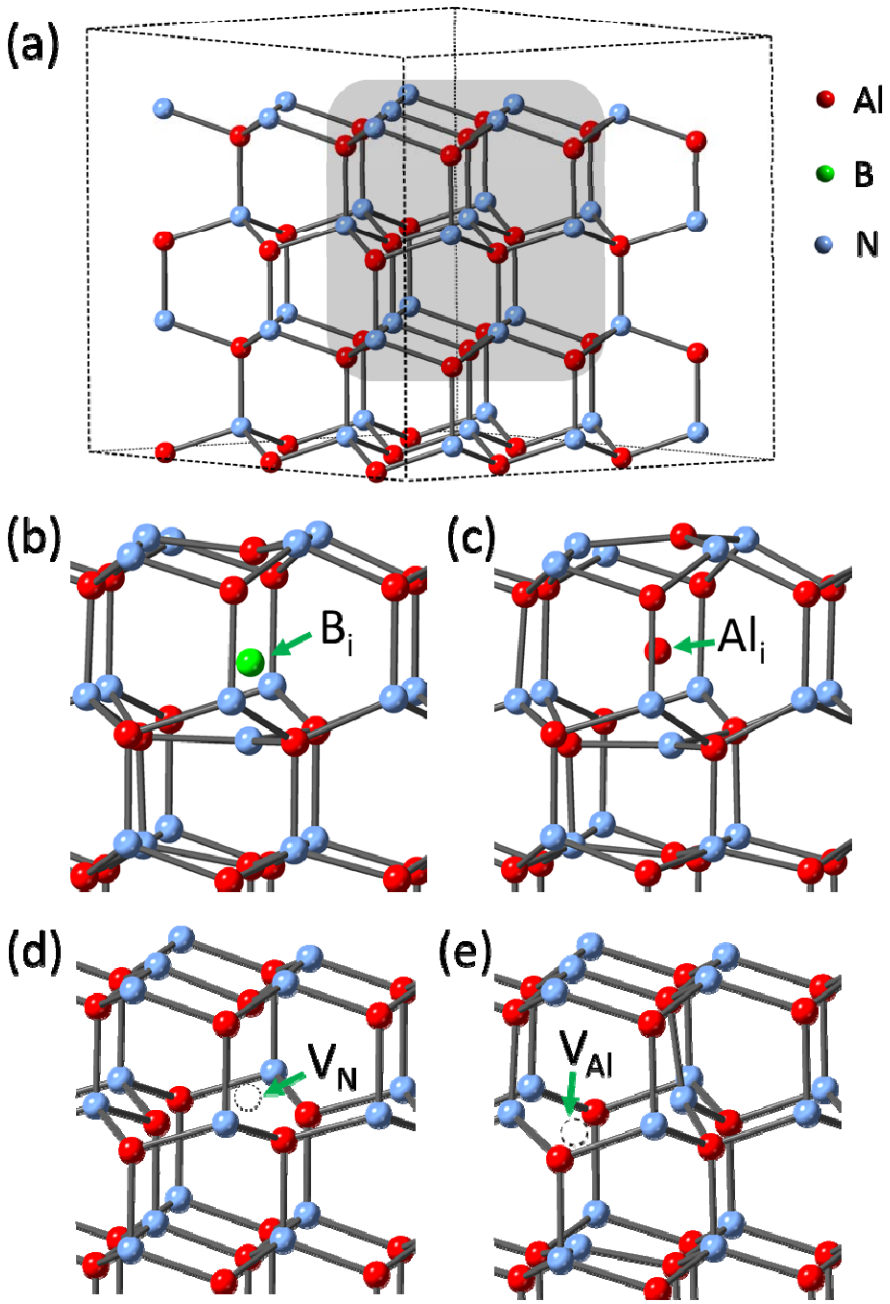

FIG. 4. (a) The 3x3x2 AlN unit cells used in DFT calculations. The shaded region is magnified to show the atomic arrangements with: (b) B interstitial; (c) Al interstitial; (d) N vacancy; and (e) Al vacancy. The point defects structures in (b)-(d) are relaxed from (a) using 3x3x3 k-points. The arrows mark the position of the defects.

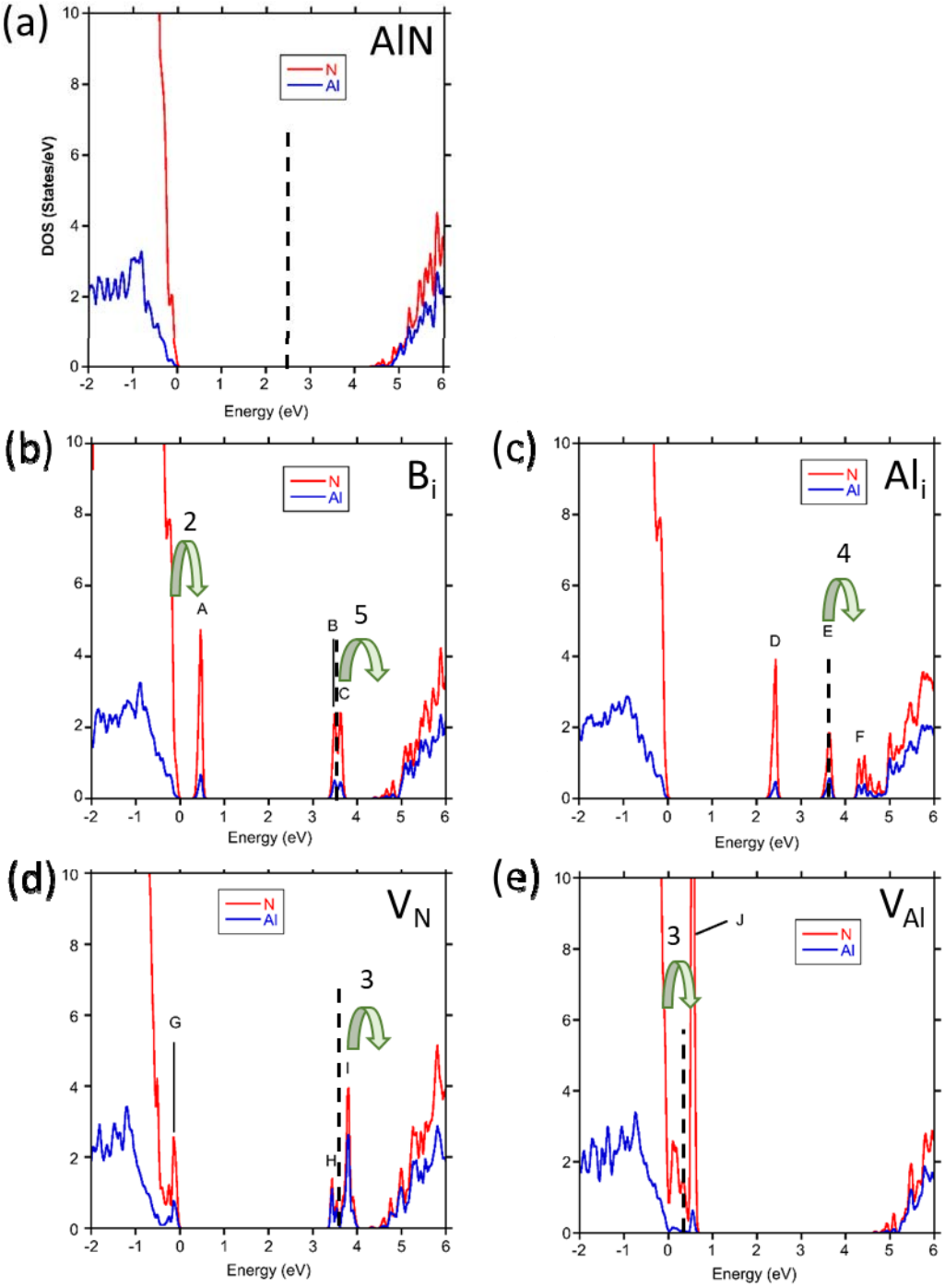

FIG. 5. DFT calculations for AlN in a 3x3x2 supercell: (a) Without point defects, (b) With single B interstitial, (c) With single Al interstitial, (d) With single N vacancy, and (e) With single Al vacancy. The defect states in the band gap are marked from A to J, and are summarized in TABLE III. The Fermi levels are marked by black dashed lines.